

Topological Floquet edge states in periodically curved waveguides

Bo Zhu,^{1,2} Honghua Zhong,^{1,3} Yongguan Ke,^{1,2} Xizhou Qin,¹ Andrey A. Sukhorukov,⁴
Yuri S. Kivshar,⁴ and Chaohong Lee^{1,2,5,*}

¹*Laboratory of Quantum Engineering and Quantum Metrology, School of Physics and Astronomy,
Sun Yat-Sen University (Zhuhai Campus), Zhuhai 519082, China*

²*State Key Laboratory of Optoelectronic Materials and Technologies, Sun Yat-Sen University (Guangzhou Campus),
Guangzhou 510275, China*

³*Institute of Mathematics and Physics, Central South University of Forestry and Technology, Changsha 410004, China*

⁴*Nonlinear Physics Centre, Research School of Physics and Engineering, The Australian National University, Canberra ACT 2601, Australia*

⁵*Synergetic Innovation Center for Quantum Effects and Applications, Hunan Normal University, Changsha 410081, China*



(Received 11 April 2018; published 31 July 2018)

We study the Floquet edge states in arrays of periodically curved optical waveguides described by the modulated Su-Schrieffer-Heeger model. Beyond the bulk-edge correspondence, our study explores the interplay between band topology and periodic modulations. By analyzing the quasienergy spectra and Zak phase, we reveal that, although topological and nontopological edge states can exist for the same parameters, they cannot appear in the same spectral gap. In the high-frequency limit, we find analytically all boundaries between the different phases and study the coexistence of topological and nontopological edge states. In contrast to unmodulated systems, the edge states appear due to either band topology or modulation-induced defects. This means that periodic modulations may not only tune the parametric regions with nontrivial topology, but may also support novel edge states.

DOI: [10.1103/PhysRevA.98.013855](https://doi.org/10.1103/PhysRevA.98.013855)

I. INTRODUCTION

Recently, topological photonics has emerged as a new approach to manipulate properties of light under continuous deformations [1]. Electromagnetic topological states have been found in both microwave [2–4] and optical [5–7] regimes. Similar to topological insulators for electrons, photonic topological insulators have also been created [1–16]. Beyond conventional topological phenomena in linear Hermitian systems, topological gap solitons have been found in nonlinear optical systems [17], and it was shown that topological states can survive in non-Hermitian systems [18]. Moreover, periodic modulations can bring several novel topological properties usually absent in their nonmodulated analogs [9,19–26].

Bulk-edge correspondence [27,28] is a well-established principle for two-dimensional (2D) topological systems. It establishes the exact correspondence between bulk states subjected to periodic boundary conditions (PBCs) and edge states in the systems with open boundary conditions (OBCs). Up to now, topological edge states have been found in several 2D photonic systems [10,13,29,30]. However, for one-dimensional (1D) lattice models, edge states have been shown to appear in periodically modulated but nontopological lattices [31,32]. This suggests that edge states can be induced by either topology or periodic modulations. Here, we wonder whether topological and nontopological edge states may coexist and, if they may coexist, how to distinguish between topological and nontopological edge states.

In this work, we study the Floquet edge states (FESs) in arrays of periodically curved optical waveguides described by a periodically modulated Su-Schrieffer-Heeger (SSH) model [33]. We analyze the interplay between band topology and periodic modulations, and describe the coexistence of both topological and nontopological edge states supported by the same parameters. Our results show that, for a specific gap, the Zak phase Z_{G_m} is either zero or π , so that the topological edge states appear only in the gap of $Z_{G_m} = \pi$. Through controlling both modulation frequency and amplitude, we may drive the system from nontopological to topological regime, and vice versa. We demonstrate analytically that periodic modulations induce a *virtual defect at the boundary*—the key mechanism for the formation of nontopological edge states.

The paper is organized as follows. In Sec. II, we introduce our physical model and derive its coupled-mode equations. In Sec. III, we calculate the quasienergy spectra under OBC. In Sec. IV, by employing the multiscale perturbation analysis, we give the effective coupled-mode equations and demonstrate that the periodic modulations can induce virtual defects at boundaries. The FESs include defect-free surface states and Shockley-like surface states, which are induced by virtual defects and the alternating strong and weak couplings between waveguides, respectively. In Sec. V, we analytically obtain the asymptotic phase boundary and numerically give the phase diagram of appearing FESs, respectively. We explore the topological nature of all FESs via the calculation of the bulk topological invariant Zak phase. We find that Shockley-like surface states are topological FESs and defect-free surface states are nontopological FESs. A brief summary is given in Sec. VI.

*Corresponding author: lichaoh2@mail.sysu.edu.cn; chleeen@gmail.com

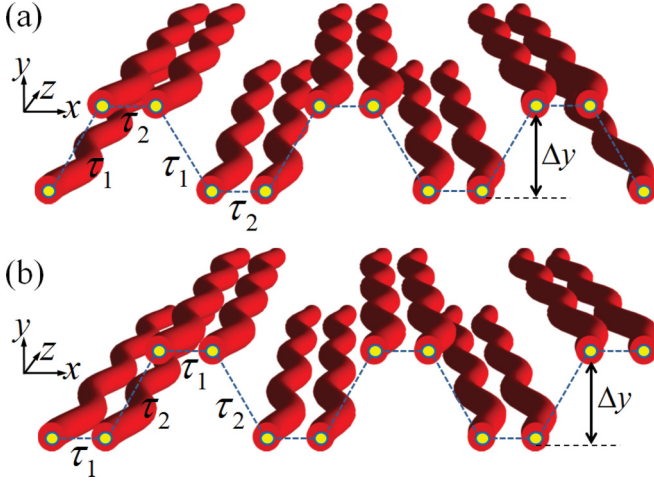


FIG. 1. Schematic diagram of waveguide arrays curved along the propagation direction of light (z axis). The center-to-center spacing along the x axis is fixed as Δx , and the one along the y axis is either zero or Δy intermittently. The coupling strength is either τ_1 or τ_2 intermittently. (a) $\tau_1/\tau_2 < 1$ with $\tau_2 = \tau$ and (b) $\tau_1/\tau_2 > 1$ with $\tau_1 = \tau$.

II. MODEL

We consider an array of coupled optical waveguides, where the waveguides are periodically curved along the longitudinal propagation direction; see Fig. 1. The light field $\psi(x, y, z)$ obeys the paraxial wave equation

$$-i \frac{\partial \psi}{\partial z} = \frac{\lambda'}{4\pi n'} \left(\frac{\partial^2}{\partial x^2} + \frac{\partial^2}{\partial y^2} \right) \psi + \frac{2\pi}{\lambda'} v(x, y, z) \psi, \quad (1)$$

where λ' is the optical wavelength in vacuum, n' is the medium refractive index, and $v(x, y, z)$ describes the refractive index at (x, y, z) . The waveguide centers $x_n(z) = x_n(z + T)$ are periodically curved along the longitudinal direction with the curving period T much larger than the interwaveguide distance Δx . Here we set $x_n(z) = n\Delta x + A[\cos(\omega z) - 1]$ with the modulation amplitude A and the modulation frequency ω .

By implementing the coordinate transformation $[\hat{z} = z, \hat{y} = y, \hat{x}(z) = x - x_0(z)]$, we have $\partial_x = \partial_{\hat{x}}, \partial_y = \partial_{\hat{y}}$, and $\partial_z = \partial_{\hat{z}} - \dot{x}_0 \partial_{\hat{x}}$. Therefore, the field $\psi(\hat{x}, \hat{y}, \hat{z})$ obeys

$$-i \frac{\partial \psi}{\partial \hat{z}} = -i \dot{x}_0 \frac{\partial \psi}{\partial \hat{x}} + \frac{2\pi}{\lambda'} v \psi + \frac{\lambda'}{4\pi n'} \left(\frac{\partial^2}{\partial \hat{x}^2} + \frac{\partial^2}{\partial \hat{y}^2} \right) \psi.$$

By applying the gauge transformation

$$\psi = \phi \exp \left\{ i \frac{\pi n'}{\lambda'} \left(2\dot{x}_0(\hat{z})\hat{x}(\hat{z}) - \int_0^{\hat{z}} \dot{x}_0^2(\xi) d\xi \right) \right\},$$

the paraxial wave equation (1) can be written as

$$-i \frac{\partial \phi}{\partial \hat{z}} = \frac{\lambda'}{4\pi n'} \left(\frac{\partial^2}{\partial \hat{x}^2} + \frac{\partial^2}{\partial \hat{y}^2} \right) \phi + \frac{2\pi}{\lambda'} v \phi - \frac{2\pi n'}{\lambda'} \ddot{x}_0 \hat{x} \phi.$$

Expanding the field into a superposition of the single-mode fields in individual waveguides

$$\phi(\hat{x}, \hat{y}, \hat{z}) = \sum_n \varphi_n(\hat{z}) a_n(\hat{x}, \hat{y}),$$

we obtain the coupled-mode equations

$$-i \frac{d\varphi_n}{d\hat{z}} = \tau_n \varphi_{n+1} + \tau_{n-1} \varphi_{n-1} + D_n \varphi_n - \eta \ddot{x}_0 n \varphi_n,$$

where $\eta = 2\pi n'/\lambda'$ as a normalized optical frequency, and

$$\tau_n = \frac{2\pi}{\lambda'} \iint a_n^*(\hat{x}, \hat{y}) v(\hat{x}, \hat{y}, \hat{z}) a_{n+1}(\hat{x}, \hat{y}) d\hat{x} d\hat{y},$$

$$D_n = \frac{2\pi}{\lambda'} \iint a_n^*(\hat{x}, \hat{y}) v(\hat{x}, \hat{y}, \hat{z}) a_n(\hat{x}, \hat{y}) d\hat{x} d\hat{y}.$$

By performing a transformation

$$\varphi_n = \exp[i\eta A \omega \hat{x}_n \sin(\omega z) + i D_n z] u_n,$$

we derive the coupled-mode equations as

$$-i \frac{du_n}{dz} = \tau_n \exp[i\eta A \omega (\hat{x}_{n+1} - \hat{x}_n) \sin(\omega z)] u_{n+1} + \tau_{n-1} \exp[-i\eta A \omega (\hat{x}_n - \hat{x}_{n-1}) \sin(\omega z)] u_{n-1}. \quad (2)$$

Here $\eta = 2\pi n'/\lambda'$; u_n denotes the complex field amplitude for the n th waveguide with n being the waveguide index. As the center-to-center waveguide spacing along the x axis is constant (i.e., $\hat{x}_{n+1} - \hat{x}_n = \hat{x}_n - \hat{x}_{n-1} = \Delta \hat{x} = 1$) and one along the y axis is either zero or Δy intermittently, the hopping strengths can be written as $\tau_n = \frac{1}{2} \{ [1 - (-1)^n] \tau_1 + [1 + (-1)^n] \tau_2 \}$ and the maximum hopping strength $\tau = \max\{\tau_1, \tau_2\}$ is fixed. By adjusting the distance $\Delta \hat{y}$, one may tune the values of τ_n .

Without loss of generality, we set $\eta = 1$ and $\tau = 1$. Therefore, the system can be described by the periodically modulated SSH-like Hamiltonian

$$H(z) = \sum_{n=1}^{2N} \{ \tau_n \exp[iA \omega \sin(\omega z)] u_n^* u_{n+1} + \text{H.c.} \}, \quad (3)$$

with $2N$ being the total number of optical waveguides. Chiral symmetry is represented by the sublattice operator $\Gamma = \sum_n u_{2n-1}^* u_{2n-1} - \sum_n u_{2n}^* u_{2n}$, which is unitary, Hermitian, and local. Obviously, $\Gamma H \Gamma = -H$; this means that this periodically modulated SSH-like Hamiltonian has chiral symmetry [34]. On the other hand, the above Hamiltonian also has time reversal symmetry, i.e., it is invariant under the transformation $[z \rightarrow -z, i \rightarrow -i]$.

III. FLOQUET ENERGY SPECTRUM

Since the system is invariant under $z \rightarrow z + T$, according to the Floquet theorem [20], the steady states of the coupled-mode equation (2) follow

$$u_n(z) = e^{-iEz} \sum_{\chi=-\infty}^{+\infty} e^{-i\chi\omega z} c_{n,\chi},$$

where $c_{n,\chi}$ is the amplitude of the χ th Floquet state. Substituting the above Floquet expansion into the coupled-mode equations, one obtains the quasienergy equation in the Floquet

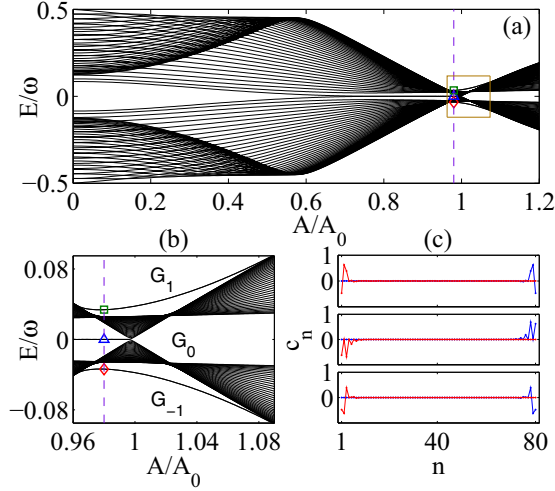


FIG. 2. Quasienergy spectra under open boundary condition. (a) Scaled quasienergy E/ω vs the scaled modulation amplitude A/A_0 . (b) Enlarged rectangular region of (a). (c) The Floquet edge states corresponding to the square, triangle, and diamond points in the three gaps (G_{+1} , G_0 , G_{-1}) at $A/A_0 = 0.98$ marked in (b). The parameters are chosen as $\tau_1/\tau_2 = 1.2$, $2\pi/\omega = 3$, $A_0\omega \simeq 2.405$ [which gives $J_0(A_0\omega) = 0$], the total lattice number $2N = 80$, and the truncation number $Y = 13$.

space:

$$\begin{aligned}
 E c_{n,\chi} = & \sum_{\chi'=-\infty}^{+\infty} \tau_{n-1} e^{-i\eta A\omega \sin(\omega z)} e^{-i(\chi'-\chi)\omega z} c_{n-1,\chi'} \\
 & + \sum_{\chi'=-\infty}^{+\infty} \tau_n e^{i\eta A\omega \sin(\omega z)} e^{-i(\chi'-\chi)\omega z} c_{n+1,\chi'} \\
 & + \sum_{\chi'=-\infty}^{+\infty} \chi' \omega e^{-i(\chi'-\chi)\omega z} c_{n,\chi'} \\
 & + \sum_{\chi' \neq \chi} e^{-i(\chi'-\chi)\omega z} E c_{n,\chi'}.
 \end{aligned}$$

We introduce the average over one modulation period for all z -dependent quantities and obtain the quasienergy eigenmode equation

$$\begin{aligned}
 E c_{n,\chi} = & \sum_{\chi'=-\infty}^{+\infty} \tau_{n-1} J_{\chi'-\chi} c_{n-1,\chi'} \\
 & + \sum_{\chi'=-\infty}^{+\infty} \tau_n J_{\chi'-\chi} c_{n+1,\chi'} + \chi \omega c_{n,\chi}, \quad (4)
 \end{aligned}$$

where $J_{\chi'-\chi}$ is the Bessel function $J_{\chi'-\chi}(A\omega)$. To obtain the quasienergy spectrum, one needs to truncate the Floquet space. In our calculation, we choose $\chi', \chi \in [-X, X]$ and $Y = 2X + 1$ is the truncation number.

Now we discuss the quasienergy spectra under OBC. In Figs. 2(a) and 2(b), we show the scaled quasienergy E/ω versus the scaled modulation amplitude A/A_0 . In our calculation, A_0 is given by the first zero point of $J_0(A_0\omega)$, $\tau_1/\tau_2 = 1.2$, $2\pi/\omega = 3$, and the total lattice number $2N = 80$. In the energy

gap G_0 , there appear isolated zero-energy levels under some parameter ranges. Because the quasienergies have periodicity in Floquet space, similar isolated levels can also appear in gaps $G_{\pm 2, \pm 4, \dots}$. In the energy gaps G_{-1} and G_1 , isolated nonzero-energy levels appear around $A/A_0 \sim 1$ and the similar isolated levels can also appear in gap $G_{\pm 3, \pm 5, \dots}$. Below, we concentrate our discussion on the quasienergy ranges $-1/2 \leq E/\omega \leq 1/2$. In particular, isolated zero- and nonzero-energy levels can coexist in the same parametric region; see Fig. 2(b). The eigenstate profiles, which localize at two edges, indicate that these isolated levels are FESs [see Fig. 2(c)]. We know that the topological edge states in a static SSH model always appear as zero-energy modes. However, in our modulated system, there appear both zero- and nonzero-energy edge states. Naturally, there arises an open question: are all FESs induced by topology?

IV. MULTISCALE ANALYSIS

To understand how FESs appear in the high-frequency limit, we employ the multiscale perturbation analysis [31,35]. We rewrite Eq. (2) as

$$-i \frac{du_n}{dz} = \sum_m W(z; n, m) u_m, \quad (5)$$

with

$$\begin{aligned}
 W(z; n, m) = & \frac{1 + (-1)^n}{2} [\delta_{n,m+1} \tau_1 e^{-iA\omega \sin(\omega z)} \\
 & + \delta_{n,m-1} \tau_2 e^{iA\omega \sin(\omega z)}] \\
 & + \frac{1 - (-1)^n}{2} [\delta_{n,m+1} \tau_2 e^{-iA\omega \sin(\omega z)} \\
 & + \delta_{n,m-1} \tau_1 e^{iA\omega \sin(\omega z)}].
 \end{aligned}$$

For the open boundary condition, we have $u_{n < 1} \equiv 0$ and $u_{n > 2N} \equiv 0$, in which $2N$ is the total lattice number. Therefore, $W(z; n, m)$ can be rewritten as

$$\begin{aligned}
 W(z; n, m) = & \frac{1 + (-1)^n}{2} [\delta_{n,m+1} \tau_1 e^{-iA\omega \sin(\omega z)} \\
 & + (1 - \delta_{n,2N}) \delta_{n,m-1} \tau_2 e^{iA\omega \sin(\omega z)}] \\
 & + \frac{1 - (-1)^n}{2} [(1 - \delta_{n,1}) \delta_{n,m+1} \tau_2 e^{-iA\omega \sin(\omega z)} \\
 & + \delta_{n,m-1} \tau_1 e^{iA\omega \sin(\omega z)}]. \quad (6)
 \end{aligned}$$

Because the waveguide axes are periodically curved along the longitudinal propagation (z direction), we have $W(z; n, m) = W(z + T; n, m)$, where $T = 2\pi/\omega$. In the high-frequency limit ($\omega \gg 1$), we can introduce a small parameter ε , which satisfies $T = O(\varepsilon)$. Thus the solution of Eq. (5) can be given as the series expansion

$$\begin{aligned}
 u_n(z) = & U_n(z_0, z_1, z_2, \dots) + \varepsilon v_n(z_{-1}, z_0, z_1, z_2, \dots) \\
 & + \varepsilon^2 w_n(z_{-1}, z_0, z_1, z_2, \dots) \\
 & + \varepsilon^3 \zeta_n(z_{-1}, z_0, z_1, z_2, \dots) + O(\varepsilon^4), \quad (7)
 \end{aligned}$$

where $z_{l'} = \varepsilon^{l'} z$. Then the differentiation is performed according to the usual convention:

$$\frac{d}{dz} = \varepsilon^{-1} \frac{\partial}{\partial z_{-1}} + \frac{\partial}{\partial z_0} + \varepsilon \frac{\partial}{\partial z_1} + \varepsilon^2 \frac{\partial}{\partial z_2} + \dots \quad (8)$$

In the series solution, the function U_n describes the averaged behavior

$$\langle u_n \rangle = U_n, \quad \left\langle \frac{du_n}{dz} \right\rangle = \frac{dU_n}{dz}, \quad (9)$$

in which the average notation

$$\langle \bullet \rangle = \varepsilon T^{-1} \int_{\varepsilon^{-1}z}^{\varepsilon^{-1}(z+T)} (\bullet)(z_{-1}) dz_{-1}.$$

It is worth noting that U_n does not depend on the “fast” variable z_{-1} ; this means that

$$\langle U_n \rangle = U_n, \quad \left\langle \frac{dU_n}{dz} \right\rangle = \frac{dU_n}{dz}. \quad (10)$$

From Eqs. (9) and (10), we have

$$\begin{aligned} \langle v_n \rangle &= \langle w_n \rangle = \langle \zeta_n \rangle \equiv 0, \\ \left\langle \frac{\partial v_n}{\partial z_{l'}} \right\rangle &= \left\langle \frac{\partial w_n}{\partial z_{l'}} \right\rangle = \left\langle \frac{\partial \zeta_n}{\partial z_{l'}} \right\rangle \equiv 0, \end{aligned} \quad (11)$$

for $l' = -1, 0, 1, 2, \dots$

Substituting Eq. (7) into Eq. (5) and collecting terms with different orders of ε , we obtain

$$-i \frac{\partial U_n}{\partial z_0} = i \frac{\partial v_n}{\partial z_{-1}} + \sum_m W(z; n, m) U_m, \quad (12)$$

for the order ε^0 . Using the conditions Eq. (10) and Eq. (11) and averaging Eq. (12), we have

$$-i \frac{\partial U_n}{\partial z_0} = \sum_m W_0(n, m) U_m, \quad (13)$$

where $W_0(n, m) = \langle W(z; n, m) \rangle$. Then substituting Eq. (13) into Eq. (12), we can obtain the equation for v_n

$$-i \frac{\partial v_n}{\partial z_{-1}} = \sum_m [W(z; n, m) - W_0(n, m)] U_m. \quad (14)$$

Thus through integrating the above equation, we derive an explicit expression for the function v_n

$$v_n = i \varepsilon^{-1} \sum_m M(z; n, m) U_m, \quad (15)$$

with $M(z; n, m) = \int [W(z; n, m) - W_0(n, m)] dz$. Here, the function M is periodic and has average zero value

$$M(z; n, m) \equiv M(z + T; n, m); \langle M(z; n, m) \rangle = 0. \quad (16)$$

For the order ε^1 , we have

$$-i \frac{\partial U_n}{\partial z_1} = i \frac{\partial v_n}{\partial z_0} + i \frac{\partial w_n}{\partial z_{-1}} + \sum_m W(z; n, m) v_m. \quad (17)$$

Substituting Eqs. (15) and (13) into Eq. (17), we obtain

$$\begin{aligned} -i \frac{\partial U_n}{\partial z_1} &= -i \varepsilon^{-1} \sum_{m,j} M(z; n, j) W_0(j, m) U_m + i \frac{\partial w_n}{\partial z_{-1}} \\ &\quad + i \varepsilon^{-1} \sum_{m,j} W(z; n, j) M(z; j, m) U_m. \end{aligned} \quad (18)$$

Using the conditions (10), (11), and (16) and averaging Eq. (18), we have

$$-i \frac{\partial U_n}{\partial z_1} = i \varepsilon^{-1} \sum_{m,j} \langle W(z; n, j) M(z; j, m) \rangle U_m. \quad (19)$$

Substituting Eq. (19) into Eq. (18), we can obtain the equation for w_n :

$$\begin{aligned} -i \frac{\partial w_n}{\partial z_{-1}} &= -i \varepsilon^{-1} \sum_{m,j} M(z; n, j) W_0(j, m) U_m \\ &\quad + i \varepsilon^{-1} \sum_{m,j} [W(z; n, j) M(z; j, m) \\ &\quad - \langle W(z; n, j) M(z; j, m) \rangle] U_m. \end{aligned} \quad (20)$$

Similarly, by performing integration, we can derive the explicit expression for w_n .

For the order ε^2 , we have

$$\begin{aligned} -i \frac{\partial U_n}{\partial z_2} &= i \frac{\partial v_n}{\partial z_1} + i \frac{\partial w_n}{\partial z_0} + i \frac{\partial \zeta_n}{\partial z_{-1}} \\ &\quad + \sum_m W(z; n, m) w_m. \end{aligned} \quad (21)$$

Using Eqs. (10) and (11) and averaging Eq. (21), we obtain

$$-i \frac{\partial U_n}{\partial z_2} = \sum_q \langle W(z; n, q) w_q \rangle, \quad (22)$$

where the second term

$$\begin{aligned} \langle W(z; n, q) w_q \rangle &= \langle [W(z; n, q) - W_0(n, q)] w_q \rangle \\ &= -\varepsilon^{-1} \left\langle M(z; n, q) \frac{\partial w_q}{\partial z_{-1}} \right\rangle. \end{aligned} \quad (23)$$

Then using Eqs. (20) and (11), we can rewrite Eq. (22) as

$$\begin{aligned} -i \frac{\partial U_n}{\partial z_2} &= \varepsilon^{-2} \sum_{q,m,j} \langle M(z; n, q) [W(z; q, j) \\ &\quad - W_0(q, j)] M(z; j, m) \rangle U_m \\ &\quad + \varepsilon^{-2} \sum_{q,m,j} \langle M(z; n, q) [W_0(q, j) M(z; j, m) \\ &\quad - M(z; q, j) W_0(j, m)] \rangle U_m. \end{aligned} \quad (24)$$

By combining Eqs. (13), (19), and (24) and using Eq. (8), we obtain a closed-form equation for U_n :

$$-i \frac{dU_n}{dz} = \sum_m W_s(n, m) U_m. \quad (25)$$

Here the effective coupling coefficients are given as

$$\begin{aligned} W_s(n, m) &= W_0(n, m) + \sum_j W_1(n, j, m) \\ &\quad + \sum_{q,j} W_2(n, q, j, m), \end{aligned} \quad (26)$$

with

$$W_0(n, m) = \langle W(z; n, m) \rangle = \frac{1 + (-1)^n}{2} [\delta_{n, m+1} \tau_1 + (1 - \delta_{n, 2N}) \delta_{n, m-1} \tau_2] J_0(\eta A \omega) + \frac{1 - (-1)^n}{2} [(1 - \delta_{n, 1}) \delta_{n, m+1} \tau_2 + \delta_{n, m-1} \tau_1] J_0(\eta A \omega),$$

$$\sum_j W_1(n, j, m) = i \sum_j \langle W(z; n, j) M(z; j, m) \rangle = 0,$$

$$\begin{aligned} \sum_{q, j} W_2(n, q, j, m) &= \sum_{q, j} \langle M(z; n, q) [W(z; q, j) - W_0(q, j)] M(z; j, m) \rangle \\ &+ \sum_{q, j} \langle M(z; n, q) [W_0(q, j) M(z; j, m) - M(z; q, j) W_0(j, m)] \rangle \\ &= \frac{1 + (-1)^n}{2} \{ \delta_{n, m+1} [(\tau_1/\tau_2)^2 - 1] (\tau_1/\tau_2) \\ &+ \delta_{n, m-1} [1 - (\tau_1/\tau_2)^2] \} \Delta \\ &+ \frac{1 - (-1)^n}{2} \{ \delta_{n, m+1} [1 - (\tau_1/\tau_2)^2] \\ &+ \delta_{n, m-1} [(\tau_1/\tau_2)^2 - 1] (\tau_1/\tau_2) \} \Delta \\ &+ \frac{\tau_1}{2\tau_2} (\delta_{n, 1} \delta_{m, 2} + \delta_{n, 2} \delta_{m, 1} \\ &+ \delta_{n, 2N} \delta_{m, 2N-1} + \delta_{n, 2N-1} \delta_{m, 2N}) \Delta, \end{aligned}$$

with

$$\begin{aligned} \Delta &= -\omega^{-2} \tau_2^3 \sum_{m \neq 0} \sum_{j \neq 0, -m} J_j(A\omega) \\ &\times J_m(A\omega) J_{j+m}(A\omega) j^{-1} m^{-1}. \end{aligned}$$

Finally, the effective equations for the slowly varying functions $U_n(z)$ read as

$$\begin{aligned} -i \frac{dU_{2n-1}}{dz} &= \tau_a U_{2n} + \tau_b U_{2n-2} + \delta_{(2n-1, 1)} \tau_c U_2 \\ &+ \delta_{(2n-1, 2N-1)} \tau_c U_{2N}, \\ -i \frac{dU_{2n}}{dz} &= \tau_b U_{2n+1} + \tau_a U_{2n-1} + \delta_{(2n, 2)} \tau_c U_1 \\ &+ \delta_{(2n, 2N)} \tau_c U_{2N-1}, \end{aligned} \quad (27)$$

with Kronecker's delta function $\delta_{(n, m)}$. Here, the effective couplings are given as

$$\begin{aligned} \tau_a &= \tau_1 J_0 - (\tau_1/\tau_2) \Theta, \\ \tau_b &= \tau_2 J_0 + \Theta, \\ \tau_c &= \tau_1 \Delta / (2\tau_2), \end{aligned} \quad (28)$$

with $\Delta = -\omega^{-2} \tau_2^3 \sum_{m \neq 0} \sum_{j \neq \{0, -m\}} J_j J_m J_{j+m} j^{-1} m^{-1}$ and $\Theta = [1 - (\tau_1/\tau_2)^2] \Delta$. The effective couplings τ_c describe the virtual defects at boundaries, as shown in the schematic diagram in Fig. 4.

Based on the above discussions, the periodically modulated system can be described by effective static SSH-like coupled-mode Eqs. (27). The major difference is the existence of virtual defects at boundaries in the effective model. Similar to a surface perturbation, the virtual defects can form defect-free surface states (or FESs) [31]. On the other hand, if $\tau_c = 0$, the static SSH-like coupled-mode equations reduce to the conventional SSH model [33] and the defect-free surface states disappear. However, the 1D conventional SSH model belonging to the BDI symmetry class [36], which satisfies time reversal and chiral symmetry, can support an Z topological index (the integer Z index can only take values zero or 1) [37]. For $|\tau_a|/|\tau_b| < 1$, this system is topologically nontrivial and has one zero-energy mode localized at each edge—the zero-energy edge mode also called Shockley-like surface states [38]. For $|\tau_a|/|\tau_b| > 1$, the system is topologically trivial with no edge modes. If change $\tau_c \neq 0$, the static SSH-like coupled-mode equations still satisfy time reversal and chiral symmetry, which illustrates that the multiscale perturbation analysis does not change the symmetry of the system. Similar to the static system, the relation between Shockley-like and Tamm-like surface states has been discussed in [38–40]. Their results show that the transitions between Shockley-like and Tamm-like surface states are observed by tuning the surface perturbation (embedded defects). In our system, without any embedded or nonlinearity-induced defects, the surface perturbation (virtual defects) is induced by periodical modulations. In the next section, we will give the parameter regions of FESs and explore their topological nature.

V. NONTOPOLOGICAL VS TOPOLOGICAL EDGE STATES

A. Asymptotic phase boundary

To estimate the cutoff values (phase boundaries) for the regions of FESs caused by virtual defects. We now consider stationary solutions in the form of $U_n(z) = U_n(0) e^{iEz}$ with E being the propagation constant. Substituting it into Eq. (27), we obtain

$$\begin{aligned} EU_{2n-1} &= \tau_a U_{2n} + \tau_b U_{2n-2} \\ &+ (\delta_{2n-1, 1} \tau_c U_2 + \delta_{2n-1, 2N-1} \tau_c U_{2N}), \\ EU_{2n} &= \tau_b U_{2n+1} + \tau_a U_{2n-1} \\ &+ (\delta_{2n, 2} \tau_c U_1 + \delta_{2n, 2N} \tau_c U_{2N-1}). \end{aligned} \quad (29)$$

For an infinite lattice, we have

$$\begin{aligned} EU_{2n-1} &= \tau_a U_{2n} + \tau_b U_{2n-2}, \\ EU_{2n} &= \tau_b U_{2n+1} + \tau_a U_{2n-1}. \end{aligned} \quad (30)$$

The solution of Eqs. (30) can be given as the ansatz

$$\begin{aligned} U_{2n-1} &= a_1 Q e^{ikn} + a_2 P e^{-ikn}, \\ U_{2n} &= a_1 P e^{ikn} + a_2 Q e^{-ikn}, \end{aligned} \quad (31)$$

where a_1 and a_2 are arbitrary nonzero constants. Substituting Eqs. (31) into Eqs. (30), we obtain

$$E \begin{bmatrix} P \\ Q \end{bmatrix} = \begin{bmatrix} 0 & \tau_a + \tau_b e^{ik} \\ \tau_a + \tau_b e^{-ik} & 0 \end{bmatrix} \begin{bmatrix} P \\ Q \end{bmatrix}. \quad (32)$$

Then we can have

$$\frac{P}{Q} = \frac{E}{\tau_a + \tau_b e^{-ik}} = \frac{\tau_a + \tau_b e^{ik}}{E}. \quad (33)$$

Therefore, the propagation constant is given as

$$E^2 = \tau_a^2 + \tau_b^2 + 2\tau_a \tau_b \cos(k), \quad (34)$$

for $k \in [-\pi, \pi]$.

For a finite but sufficiently large number of lattices ($2N = 80$ in our calculation), considering the two edges, we have

$$\begin{aligned} EU_2 &= (\tau_a + \tau_c)U_1 + \tau_b U_3, \\ EU_1 &= (\tau_a + \tau_c)U_2, \\ EU_{2N} &= (\tau_a + \tau_c)U_{2N-1}, \\ EU_{2N-1} &= (\tau_a + \tau_c)U_{2N} + \tau_b U_{2N-2}. \end{aligned} \quad (35)$$

Besides U_1 and U_{2N} , the coupling equations are consistent with Eqs. (30). So that we should rewrite the ansatz, similar to Eqs. (31), we have

$$\begin{aligned} U_{2n-1} &= U_1 \quad (n = 1), \\ U_{2n-1} &= a_1 Q e^{ikn} + a_2 P e^{-ikn} \quad (1 < n \leq N), \\ U_{2n} &= a_1 P e^{ikn} + a_2 Q e^{-ikn} \quad (1 \leq n < N), \\ U_{2n} &= U_{2N} \quad (n = N). \end{aligned} \quad (36)$$

First, we consider the left boundary of lattices and we can give a set of equations

$$\begin{aligned} EU_2 &= (\tau_a + \tau_c)U_1 + \tau_b U_3, \\ EU_1 &= (\tau_a + \tau_c)U_2, \\ EU_{2(N-1)} &= \tau_a U_{2(N-1)-1} + \tau_b U_{2(N-1)+1}. \end{aligned} \quad (37)$$

Combining Eqs. (36) and Eqs. (37), we have

$$\begin{aligned} &\frac{e^{-ik2(N-1)}}{e^{ik2(N-1)}} \\ &= \frac{[\tau_b \frac{P}{Q} e^{-ik} + \frac{(\tau_a + \tau_c)^2}{E} - E](E \frac{P}{Q} - \tau_b e^{ik} - \tau_a e^{-ik})}{[E \frac{P}{Q} - \tau_b e^{ik} - \frac{(\tau_a + \tau_c)^2}{E} \frac{P}{Q}](\tau_b \frac{P}{Q} e^{-ik} - E + \tau_a \frac{P}{Q} e^{ik})}. \end{aligned} \quad (38)$$

We set $k = -i\varrho$ and have $\frac{e^{-ik2(N-1)}}{e^{ik2(N-1)}} = e^{-4\varrho(N-1)}$, where ϱ is a real number. If $\varrho > 0$, when $N \rightarrow \infty$ we have $e^{-4\varrho(N-1)} \simeq 0$ and equivalent to

$$\left[\tau_b \frac{P}{Q} e^{-\varrho} + \frac{(\tau_a + \tau_c)^2}{E} - E \right] \left(E \frac{P}{Q} - \tau_b e^{\varrho} - \tau_a e^{-\varrho} \right) \simeq 0. \quad (39)$$

If $\varrho < 0$, when $N \rightarrow \infty$ we have $e^{-4\varrho(N-1)} \simeq \infty$ and equivalent to

$$\begin{aligned} &\left[E \frac{P}{Q} - \tau_b e^{\varrho} - \frac{(\tau_a + \tau_c)^2}{E} \frac{P}{Q} \right] \\ &\times \left(\tau_b \frac{P}{Q} e^{-\varrho} - E + \tau_a \frac{P}{Q} e^{\varrho} \right) \simeq 0. \end{aligned} \quad (40)$$

Combining Eq. (33) and Eq. (39), we have

$$e^{\varrho} = \frac{\tau_c(\tau_c + 2\tau_a)}{\tau_a \tau_b} = e^{ik} = d. \quad (41)$$

Similarly, combining Eq. (33) and Eq. (40), we have

$$e^{-\varrho} = \frac{\tau_a \tau_b}{\tau_c(\tau_c + 2\tau_a)} = e^{-ik} = d^{-1}. \quad (42)$$

Thus in the vicinity of the self-collimation point [$J_0(A_0\omega) = 0$], as the couplings (τ_a, τ_b) are very weak, the edge states induced by the virtual defects with the quasienergies E_s are given as

$$\begin{aligned} E_s^2 &= \tau_a^2 + \tau_b^2 + \tau_a \tau_b [e^{ik} + e^{-ik}] \\ &= \tau_a^2 + \tau_b^2 + \tau_a \tau_b [d + d^{-1}]. \end{aligned} \quad (43)$$

On the other hand, when we consider the right boundary of lattices, we can also obtain the surface energy E_s which is in agreement with Eq. (43).

Obviously, when $E_s^2 > \max(E^2)$, FESs appear in the energy gaps G_{-1} and G_1 . Otherwise, when $E_s^2 < \min(E^2)$, FESs appear in the gap G_0 . Obviously, $\max(E^2)$ and $\min(E^2)$ are given by $|\cos(k)| = 1$. From $\cos(k) = +1$, one can obtain the cutoff values

$$A_{cs}^{1,2}/A_0 \simeq 1 - \frac{\tau_1 \tilde{\tau}_c \pm F_a}{\tau_1 \tau_2}. \quad (44)$$

From $\cos(k) = -1$, one can obtain the cutoff values

$$A_{cs}^{3,4}/A_0 \simeq 1 - \frac{-\tau_1 \tilde{\tau}_c \pm F_b}{\tau_1 \tau_2}. \quad (45)$$

Here, A_0 is the first root of the Bessel function $J_0(A\omega) = 0$, $F_a = \sqrt{(\tau_1 \tilde{\tau}_c)^2 + \tau_1 \tau_2 M_+}$, $F_b = \sqrt{(\tau_1 \tilde{\tau}_c)^2 + \tau_1 \tau_2 M_-}$, $\tilde{\tau}_c = \frac{\tau_1}{2\tau_2} \tilde{\Delta}$, $M_{\pm} = \frac{\tau_1}{\tau_2} [1 - (\frac{\tau_1}{\tau_2})^2] \tilde{\Delta} \{ [1 - (\frac{\tau_1}{\tau_2})^2] \tilde{\Delta} \mp 2\tilde{\tau}_c \} \pm (\tilde{\tau}_c)^2$, and $\tilde{\Delta} = \Delta|_{A \rightarrow A_0}$. These cutoff values define the boundaries between the regions with and without FESs; see the dashed blue curves in Figs. 4(a) and 4(b), which are also called defect-free surface states [31]. Since F_b is a purely imaginary number for all $2\pi/\omega$ when $\tau_1/\tau_2 = 1.2$, in Fig. 4(a), there are no cutoff values $A_{cs}^{3,4}/A_0$. When $2\pi/\omega \rightarrow 0$, all cutoff values gradually converge into one point at $A/A_0 = 1$, and there are no FESs caused by the virtual defects.

On the other hand, as the effective model Eq. (27) is an SSH-like model, the system changes from topological to non-topological when the effective coupling is tuned from $|\tau_a| < |\tau_b|$ to $|\tau_a| > |\tau_b|$. The effective couplings (τ_a, τ_b) depend on the original couplings (τ_1, τ_2) and the driving parameters (A, ω). We show the effective coupling strengths ($|\tau_a|, |\tau_b|$) versus the scaled modulation amplitude A/A_0 for $2\pi/\omega = 2$ and $\tau_1/\tau_2 = 1.2$; see the inset in Fig. 4(a). There appear two intersection points at $|\tau_a| = |\tau_b|$ when A/A_0 increases. In the regions of $|\tau_a| < |\tau_b|$, topological FESs appear (the relevant cumulative phase being π), which is also called Shockley-like surface states [38]. The intersection points, where topological phase transition points occur, are given by

$$A_{ct}^{5,6}/A_0 \simeq 1 + \frac{(1 \pm \tau_1/\tau_2)^2 \tilde{\Delta}}{\tau_2}. \quad (46)$$

See the dashed blue curves 5 and 6 in the inset of Fig. 4(b). Similarly, when $2\pi/\omega \rightarrow 0$, these two curves also gradually converge into one point at $A/A_0 = 1$. Thus, in the limit of $2\pi/\omega = 0$, the effective couplings vanish when $A/A_0 = 1$ and the modulation does not change the topological feature when A/A_0 is tuned through $A/A_0 = 1$.

B. Zak phase

To distinguish topological and nontopological FESs, we calculate the bulk topological invariant—the Zak phase [41]. The Zak phase can predict the existence (with the relevant cumulative phase being π) or absence (vanishing cumulative phase) of topological FESs in specific gaps.

For a modulated SSH system of N cells (i.e., $2N$ lattices) under PBC, by implementing a Fourier transform

$$\begin{aligned} c_{2n-1,\chi} &= \frac{1}{\sqrt{N}} \sum_k e^{ik(2n-1)} c_{1,k,\chi}, \\ c_{2n,\chi} &= \frac{1}{\sqrt{N}} \sum_k e^{ik2n} c_{2,k,\chi}, \end{aligned} \quad (47)$$

we obtain the quasienergy spectra and the eigenstates by diagonalizing the quasienergy equation

$$E_l \begin{pmatrix} c_{1,k,\chi}^{(l)} \\ c_{2,k,\chi}^{(l)} \end{pmatrix} = \sum_{\chi'} \hat{\mathcal{R}}(k) \begin{pmatrix} c_{1,k,\chi'}^{(l)} \\ c_{2,k,\chi'}^{(l)} \end{pmatrix} + \chi \omega \hat{I} \begin{pmatrix} c_{1,k,\chi}^{(l)} \\ c_{2,k,\chi}^{(l)} \end{pmatrix},$$

with the 2×2 unit matrix \hat{I} and the matrix

$$\hat{\mathcal{R}}(k) = \begin{pmatrix} 0 & P_F(k) \\ \tilde{P}_F(k) & 0 \end{pmatrix}.$$

Here, $P_F = \tau_1 J_{\chi'-\chi} e^{ik} + \tau_2 J_{\chi-\chi'} e^{-ik}$, $\tilde{P}_F = \tau_1 J_{\chi-\chi'} e^{-ik} + \tau_2 J_{\chi'-\chi} e^{ik}$, and k denotes the quasimomentum.

To compute the Zak phase for the Floquet quasienergy spectrum one needs to truncate the Floquet space. The number of replicas needs to be chosen so that all relevant transitions at the desired energy are kept. The Zak phase Z_{G_m} for a specific gap is given by summing up $Z^{(l)}$ for all bands below the gap, where $Z^{(l)} = i \oint_k \langle c_k^{(l)} | \partial_k | c_k^{(l)} \rangle dk$ and the eigenstates $|c_k^{(l)}\rangle = \sum_{\alpha,\chi} c_{\alpha,k,\chi}^{(l)} |\alpha, k, \chi\rangle$ for the l th band are superposition states of different Floquet-Bloch states $|\alpha, k, \chi\rangle$. For a gap between the $(Y+m)$ th and $(Y+m+1)$ th bands, its Zak phase Z_{G_m} is defined as

$$Z_{G_m} = \sum_{l=1}^{Y+m} Z^{(l)} = \sum_{l=1}^{Y+m} \left[i \oint_k \langle c_k^{(l)} | \partial_k | c_k^{(l)} \rangle dk \right]. \quad (48)$$

For example, the Zak phase Z_{G_1} can be calculated by summing up all $Z^{(l)}$ for the bands below the gap G_1 ; see in Fig. 3.

C. Phase diagram

To verify the above analytical results, we numerically calculate the quasienergy spectra. From the quasienergy spectra under OBC, we indeed find several FESs appear. We then calculate Zak phases of the corresponding bulk states under PBC and find that the Zak phase Z_{G_m} for a specific gap is either zero or π and topological FESs only appear in a gap of nonzero Z_{G_m} .

In Fig. 4, we show the phase diagram of all possible FESs in the parameter plane $(2\pi/\omega, A/A_0)$. The appearance of topological FESs (red regions) and nontopological FESs (yellow regions) and their coexistence (mesh regions) sensitively depends on the coupling ratio τ_1/τ_2 and the modulation parameters $(\omega, A/A_0)$. In the absence of modulation, topological edge states appear only if $\tau_1/\tau_2 < 1$; otherwise, no

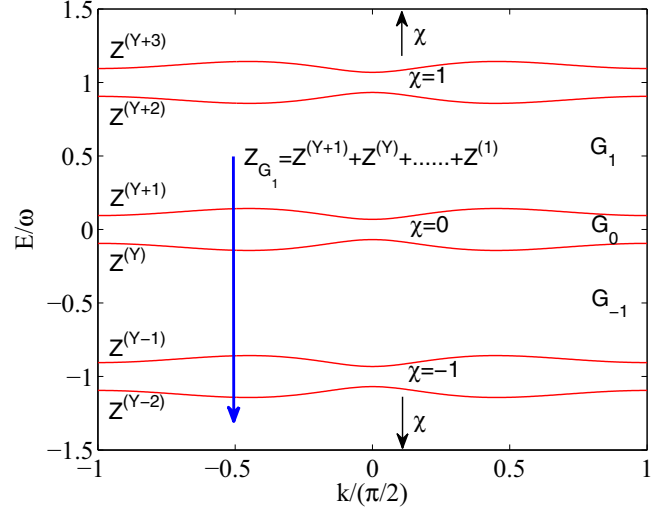


FIG. 3. Quasienergy spectrum in the quasimomentum space and the Zak phase for the gap G_1 .

edge state appears. However, by applying a proper modulation, topological FESs may appear even if $\tau_1/\tau_2 > 1$ and also may disappear even if $\tau_1/\tau_2 < 1$. In addition to the regions of topological and nontopological FESs, there exists the region of no edge states. When $2\pi/\omega \rightarrow 0$, topological FESs appear if $\tau_1/\tau_2 < 1$ and all nontopological FESs gradually vanish at the zero point of the Bessel function $J_0(A_0\omega) = 0$. Our numerical results clearly show all phase boundaries (the solid curves) gradually converge into one point at $A/A_0 = 1$ when $2\pi/\omega \rightarrow 0$, which well agree with our analytical results (the dashed blue curves).

D. Noncoexistence of nontopological and topological Floquet edge states in the same gap

Although nontopological and topological FESs can be supported by the same parameters, we find that they cannot appear in the same energy gap. In this section, we only consider the quasienergy ranges $-1/2 \leq E/\omega \leq 1/2$, so that the topological FESs (Zak phase $Z_{G_0} = \pi$) only possibly appear in gap G_0 . We will prove that nontopological and topological FESs cannot coexist in the gap G_0 . For the whole Floquet spaces, due to the periodicity of quasienergy, this proves indirect reflection the topological FESs cannot appear in the gap $G_{\pm 1, \pm 3, \pm 5, \dots}$; in addition the nontopological and topological FESs cannot coexist in the gap $G_{0, \pm 2, \pm 4, \dots}$.

If nontopological FESs appear in the gap G_0 , the edge state quasienergy E_s and the bulk-state quasienergy E will satisfy the condition $E_s^2 < \min(E^2)$. From Eq. (34), the condition $E_s^2 < \min(E^2)$ reads

$$E_s^2 < \min(\tau_a^2 + \tau_b^2 - 2\tau_a\tau_b, \tau_a^2 + \tau_b^2 + 2\tau_a\tau_b), \quad (49)$$

which requests the parameters obeying $\tau_c(\tau_c + 2\tau_a) < 0$. As the nontopological FESs appear around $A/A_0 \sim 1$, we have $\tau_c = \frac{\tau_1}{2\tau_2} \Delta < 0$, so that the above inequality is equivalent to

$$2\tau_1 J_0(A\omega) - 2\frac{\tau_1}{\tau_2} \left[1 - \left(\frac{\tau_1}{\tau_2} \right)^2 \right] \Delta + \frac{1}{2} \left(\frac{\tau_1}{\tau_2} \right) \Delta > 0. \quad (50)$$

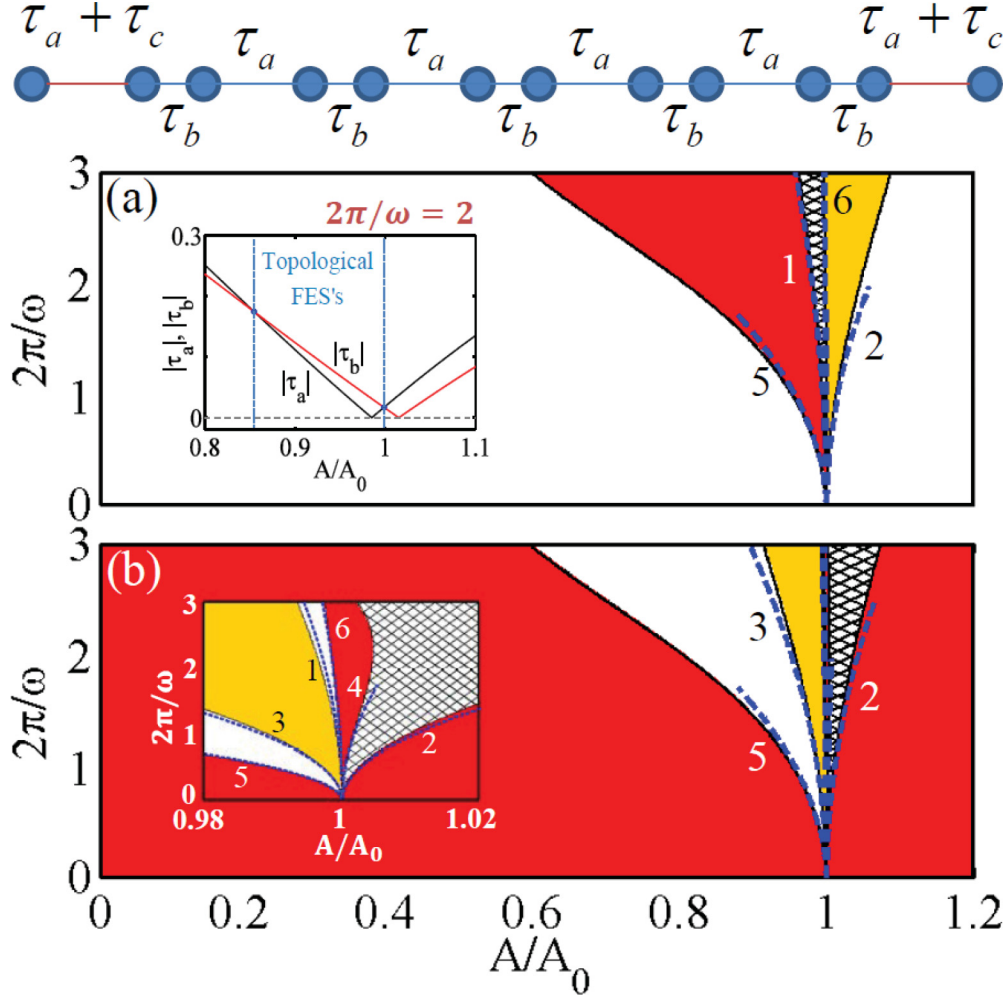


FIG. 4. Phase diagram of the Floquet edge states. Top: schematic diagram for the effective model Eq. (27). (a),(b) Phase diagrams for (a) $\tau_1/\tau_2 = 1.2$ and (b) $\tau_2/\tau_1 = 1.2$. The red regions only support topological FESs, the yellow regions only support nontopological FESs, and the mesh regions support both topological and nontopological FESs. The curves 1, 2, 3, and 4 respectively correspond to the nontopological FES cutoff values A_{cs}^1/A_0 , A_{cs}^2/A_0 , A_{cs}^3/A_0 , and A_{cs}^4/A_0 , while the curves 5 and 6 respectively correspond to the topological transition points A_{ct}^5/A_0 and A_{ct}^6/A_0 , where the inset in (b) is the enlarged region nearby $A/A_0 \sim 0$. The system changes from topological to nontopological when the effective couplings are tuned from $|\tau_a| < |\tau_b|$ to $|\tau_a| > |\tau_b|$; see the inset in (a) for $2\pi/\omega = 2$.

Below we separately discuss the two cases: (I) $\tau_2 > \tau_1 > 0$ and (II) $\tau_1 > \tau_2 > 0$.

Case I: $\tau_2 > \tau_1 > 0$. Without loss of generality, one can set $\tau_2 = 1$.

As $\tau_a < 0$ always contradicts the condition (50), the appearance of nontopological FESs in the gap G_0 requests

$$\begin{aligned} \tau_a &= \tau_1 J_0(A\omega) - \tau_1[1 - (\tau_1)^2]\Delta > 0, \\ \tau_b &= J_0(A\omega) + [1 - (\tau_1)^2]\Delta < 0, \\ 2\tau_1 J_0(A\omega) - 2\tau_1[1 - (\tau_1)^2]\Delta + \frac{1}{2}\tau_1\Delta &> 0 \end{aligned} \quad (51)$$

or

$$\begin{aligned} \tau_a &= \tau_1 J_0(A\omega) - \tau_1[1 - (\tau_1)^2]\Delta > 0, \\ \tau_b &= J_0(A\omega) + [1 - (\tau_1)^2]\Delta > 0, \\ 2\tau_1 J_0(A\omega) - 2\tau_1[1 - (\tau_1)^2]\Delta + \frac{1}{2}\tau_1\Delta &> 0. \end{aligned} \quad (52)$$

On the other hand, in the vicinity of A_0 , we have $J_0(A\omega) < 0$ when $A \rightarrow A_0^+$ and $J_0(A\omega) > 0$ when $A \rightarrow A_0^-$. Therefore, from the condition (51), one can obtain (C1) ($0 < \tau_1 < \sqrt{1-F}$) \cap ($0 < \tau_1 < \sqrt{3/4+F}$) when $A \rightarrow A_0^-$ and (C2) ($0 < \tau_1 < \sqrt{3/4+F}$) when $A \rightarrow A_0^+$. Here, the parameter F is given as $F = \frac{\omega^2 J_0(A\omega)}{4J_1^2(A\omega)J_2(A\omega)}$. However, under the condition (C2), one can find that $E_s^2 < 0$; this means that the condition (C2) does not support nontopological FESs in the gap G_0 . As we always have $\tau_b < 0$ when $A \rightarrow A_0^+$, from the condition (52), we drive the condition (C3): ($\sqrt{1-F} < \tau_1 < \sqrt{3/4+F}$) when $A \rightarrow A_0^-$. Therefore, the appearance of nontopological FESs in the gap G_0 always request $A \rightarrow A_0^-$ (where $\tau_a > 0$).

As the effective model (27) is a SSH-like model, under the condition of $|\tau_a|/|\tau_b| < 1$, the topological FESs are zero-energy modes and always appear in the gap G_0 . When $A \rightarrow A_0^-$ (where $\tau_a > 0$), from $|\tau_a|/|\tau_b| < 1$, one can obtain (D1) ($0 < \tau_1 < 1 - \sqrt{F}$) for $\tau_b < 0$ and (D2) ($0 < \tau_1 < \sqrt{F} - 1$) for

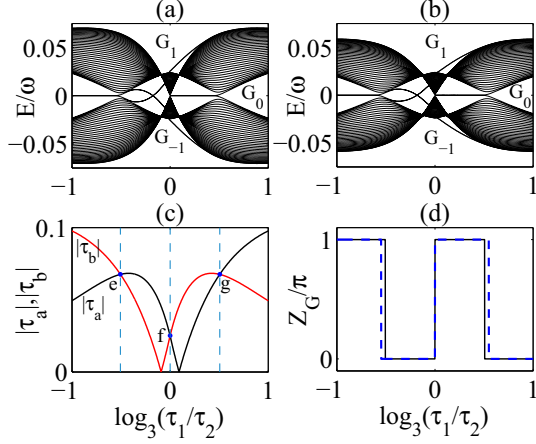


FIG. 5. Scaled quasienergy E/ω vs coupling ratio τ_1/τ_2 . (a) Band-gap structure of the effective model (27). (b) Band-gap structure of the original model (2). (c) Effective coupling strengths ($|\tau_a|$, $|\tau_b|$) vs the coupling ratio τ_1/τ_2 . (d) The Zak phases for the gap G_0 , in which the black and dashed blue lines correspond to the effective and original models, respectively. The parameters are chosen as $A/A_0 = 0.98$, $2\pi/\omega = 3$, $A_0\omega \simeq 2.405$, the total lattice $2N = 80$, and the truncation number $Y = 13$.

$\tau_b > 0$. However, under the conditions (D1) and (D2), one can find that $E_s^2 < 0$, which means the absence of nontopological FESs. That is to say, the nontopological and topological FESs cannot coexist in the gap G_0 .

Case II: $\tau_1 > \tau_2 > 0$. Without loss of generality, one can set $\tau_1 = 1$.

As $\tau_a < 0$ always contradicts the condition (50), the existence of nontopological FESs in the gap G_0 requests $\tau_a > 0$. On the other hand, in the vicinity of A_0 , we have $J_0(A\omega) < 0$ when $A \rightarrow A_0^+$ and $J_0(A\omega) > 0$ when $A \rightarrow A_0^-$. When $\tau_1 > \tau_2 > 0$, we always have $\tau_a < 0$ when $A \rightarrow A_0^+$, so that the appearance of nontopological FESs in the gap G_0 always requests $A \rightarrow A_0^-$. Moreover, when $A \rightarrow A_0^-$, we always have $\tau_b = \tau_2 J_0(A\omega) + [1 - (\frac{1}{\tau_2})^2]\Delta > 0$. Thus the appearance of nontopological FESs in the gap G_0 requests

$$\begin{aligned}\tau_a &= J_0(A\omega) - \frac{1}{\tau_2} \left[1 - \left(\frac{1}{\tau_2} \right)^2 \right] \Delta > 0, \\ \tau_b &= \tau_2 J_0(A\omega) + \left[1 - \left(\frac{1}{\tau_2} \right)^2 \right] \Delta > 0, \\ 2J_0(A\omega) - 2\frac{1}{\tau_2} \left[1 - \left(\frac{1}{\tau_2} \right)^2 \right] \Delta + \frac{1}{2} \left(\frac{1}{\tau_2} \right) \Delta &> 0.\end{aligned}\quad (53)$$

The above condition (53) requests $(\frac{2}{\sqrt{3}}\sqrt{1-F} < \tau_2 < 1)$. However, under this condition, one can find that $E_s^2 < 0$, which means the absence of nontopological FESs. This means that nontopological FESs cannot appear in gap G_0 when $\tau_1 > \tau_2 > 0$ and so there is no coexistence of nontopological and topological FESs.

In order to explore how the ratio τ_1/τ_2 affects the FESs, we show how the scaled quasienergy spectrum depends on τ_1/τ_2 . The quasienergy spectra and Zak phases show that, even when the modulation frequency is not very high, the effective model may well explain the behaviors in the original system. The devi-

ation between the effective and original models decreases with the modulation frequency and gradually vanishes in the high-frequency limit. In Fig. 5, we show the quasienergy spectra, the effective couplings, and Zak phases for $A/A_0 = 0.98$ and $2\pi/\omega = 3$. Although the quasienergies have small differences, the band-gap structures are almost the same, in which both zero and nonzero FESs may appear in different gaps; see Figs. 5(a) and 5(b). From the effective model, topological FESs are always zero-energy modes and only appear in the gap G_0 when $|\tau_a|/|\tau_b| < 1$; see Figs. 5(a) and 5(c). In addition to the topological FESs, due to the modulation-induced virtual defects, there also exist nontopological FESs in different gaps. Moreover, the band-gap structures show that topological and nontopological FESs cannot appear in the same gap, which confirms our previous analytical analysis. From the Zak phases, the effective and original models show similar topological phase transitions, but the transition points show small deviations dependent upon the modulation frequency; see Fig. 5(d).

VI. CONCLUSION

In summary, we have studied the Floquet edge states in arrays of curved optical waveguides described by the periodically modulated SSH model. According to the Floquet theorem, we give the quasienergy spectra under OBC and find several FESs. To understand how FESs appear, we employ the multiscale perturbation analysis and find the periodic modulations can induce virtual defects at boundaries. Similar to a surface perturbation, the virtual defects can form FESs (defect-free surface states) [31]. On the other hand, by changing the ratio of $|\tau_a|/|\tau_b|$, one can also obtain FESs (Shockley-like surface states).

In order to explore the topological nature of all FESs, we have calculated the quasienergy spectra and the Zak phases. Our results indicate that the Shockley-like surface state is a topological FES and the defect-free surface state is a nontopological FES. However, in our system, although topological and nontopological edge states can exist for the same parameters, they cannot appear in the same spectral gap. Without any embedded or nonlinearity-induced defects, these edge states originate from the interplay between the bulk band topology and periodic modulations. We have derived analytically the boundaries between different topological phases and have verified these results numerically. We believe our work provides perspectives for topological photonics governed by periodic modulations, and can be employed for a control of topological phase transitions. Although our analysis has been performed for arrays of periodically curved optical waveguides, it can be applicable to other lattice systems such as ultracold atoms in optical lattices [42,43], photonic crystals [18], and discrete quantum walks [44,45].

At last, we would like to point out that, if a local defect is introduced, unlike our Floquet edge states, topological and nontopological edge states may appear in the same spectral gap [46].

ACKNOWLEDGMENTS

This work was supported by the National Natural Science Foundation of China (NNSFC) under Grants No. 11574405 and No. 11465008, and by the Australian Research Council.

Both B.Z. and H.Z. made equal contributions.

- [1] L. Lu, J. D. Joannopoulos, and M. Soljačić, Topological photonics, *Nat. Photon.* **8**, 821 (2014).
- [2] F. D. M. Haldane and S. Raghu, Possible Realization of Directional Optical Waveguides in Photonic Crystals with Broken Time-reversal Symmetry, *Phys. Rev. Lett.* **100**, 013904 (2008).
- [3] S. Raghu and F. D. M. Haldane, Analogs of quantum-Hall-effect edge states in photonic crystals, *Phys. Rev. A* **78**, 033834 (2008).
- [4] Z. Wang, Y. D. Chong, J. D. Joannopoulos, and M. Soljačić, Observation of unidirectional backscattering-immune topological electromagnetic states, *Nature (London)* **461**, 772 (2009).
- [5] R. O. Umucalilar and I. Carusotto, Artificial gauge field for photons in coupled cavity arrays, *Phys. Rev. A* **84**, 043804 (2011).
- [6] K. J. Fang, Z. F. Yu, and S. H. Fan, Realizing effective magnetic field for photons by controlling the phase of dynamic modulation, *Nat. Photon.* **6**, 782 (2012).
- [7] A. B. Khanikaev, S. H. Mousavi, W. K. Tse, M. Kargarian, A. H. MacDonald, and G. Shvets, Photonic topological insulators, *Nat. Mater.* **12**, 233 (2013).
- [8] Y. E. Kraus, Y. Lahini, Z. Ringel, M. Verbin, and O. Zilberberg, Topological States and Adiabatic Pumping in Quasicrystals, *Phys. Rev. Lett.* **109**, 106402 (2012).
- [9] M. C. Rechtsman, J. M. Zeuner, Y. Plotnik, Y. Lumer, D. Podolsky, F. Dreisow, S. Nolte, M. Segev, and A. Szameit, Photonic Floquet topological insulators, *Nature (London)* **496**, 196 (2013).
- [10] M. Hafezi, S. Mittal, J. Fan, A. Migdall, and J. M. Taylor, Imaging topological edge states in silicon photonics, *Nat. Photon.* **7**, 1001 (2013).
- [11] G. Q. Liang and Y. D. Chong, Optical Resonator Analog of a Two-dimensional Topological Insulator, *Phys. Rev. Lett.* **110**, 203904 (2013).
- [12] M. Pasek and Y. D. Chong, Network models of photonic Floquet topological insulators, *Phys. Rev. B* **89**, 075113 (2014).
- [13] W. C. Hu, J. C. Pillay, K. Wu, M. Pasek, P. P. Shum, and Y. D. Chong, Measurement of a Topological Edge Invariant in a Microwave Network, *Phys. Rev. X* **5**, 011012 (2015).
- [14] L. H. Wu and X. Hu, Scheme for Achieving a Topological Photonic Crystal by Using Dielectric Material, *Phys. Rev. Lett.* **114**, 223901 (2015).
- [15] C. He, X. C. Sun, X. P. Liu, M. H. Lu, Y. Chen, L. Feng, and Y. F. Chen, Photonic topological insulator with broken time-reversal symmetry, *Proc. Natl. Acad. Sci. U.S.A.* **113**, 4924 (2016).
- [16] F. Gao, Z. Gao, X. H. Shi, Z. J. Yang, X. Lin, H. Y. Xu, J. D. Joannopoulos, M. Soljačić, H. S. Chen, L. Lu, Y. D. Chong, and B. L. Zhang, Probing topological protection using a designer surface plasmon structure, *Nat. Commun.* **7**, 11619 (2016).
- [17] Y. Lumer, Y. Plotnik, M. C. Rechtsman, and M. Segev, Self-localized States in Photonic Topological Insulators, *Phys. Rev. Lett.* **111**, 243905 (2013).
- [18] J. M. Zeuner, M. C. Rechtsman, Y. Plotnik, Y. Lumer, S. Nolte, M. S. Rudner, M. Segev, and A. Szameit, Observation of a Topological Transition in the Bulk of a Non-Hermitian System, *Phys. Rev. Lett.* **115**, 040402 (2015).
- [19] M. S. Rudner, N. H. Lindner, E. Berg, and M. Levin, Anomalous Edge States and the Bulk-edge Correspondence for Periodically Driven Two-dimensional Systems, *Phys. Rev. X* **3**, 031005 (2013).
- [20] A. Gomez-Leon and G. Platero, Floquet-Bloch Theory and Topology in Periodically Driven Lattices, *Phys. Rev. Lett.* **110**, 200403 (2013).
- [21] A. P. Slobozhanyuk, A. N. Poddubny, A. E. Miroshnichenko, P. A. Belov, and Yu. S. Kivshar, Subwavelength Topological Edge States in Optically Resonant Dielectric Structures, *Phys. Rev. Lett.* **114**, 123901 (2015).
- [22] C. Poli, M. Bellec, U. Kuhl, F. Mortessagne, and H. Schomerus, Selective enhancement of topologically induced interface states in a dielectric resonator chain, *Nat. Commun.* **6**, 6710 (2015).
- [23] D. Leykam, M. C. Rechtsman, and Y. D. Chong, Anomalous Topological Phases and Unpaired Dirac Cones in Photonic Floquet Topological Insulators, *Phys. Rev. Lett.* **117**, 013902 (2016).
- [24] Y. G. Ke, X. Z. Qin, F. Mei, H. H. Zhong, Yu. S. Kivshar, and C. Lee, Topological phase transitions and Thouless pumping of light in photonic waveguide arrays, *Laser Photon. Rev.* **10**, 995 (2016).
- [25] L. J. Maczewsky, J. M. Zeuner, S. Nolte, and A. Szameit, Observation of photonic anomalous Floquet topological insulators, *Nat. Commun.* **8**, 13756 (2017).
- [26] S. Mukherjee, A. Spracklen, M. Valiente, E. Andersson, P. Ohberg, N. Goldman, and R. R. Thomson, Experimental observation of anomalous topological edge modes in a slowly driven photonic lattice, *Nat. Commun.* **8**, 13918 (2017).
- [27] Y. Hatsugai, Chern Number and Edge States in the Integer Quantum Hall Effect, *Phys. Rev. Lett.* **71**, 3697 (1993).
- [28] Y. Hatsugai, Edge states in the integer quantum Hall effect and the Riemann surface of the Bloch function, *Phys. Rev. B* **48**, 11851 (1993).
- [29] M. Hafezi, Measuring Topological Invariants in Photonic Systems, *Phys. Rev. Lett.* **112**, 210405 (2014).
- [30] S. Mittal, S. Ganeshan, J. Y. Fan, A. Vaezi, and M. Hafezi, Measurement of topological invariants in a 2D photonic system, *Nat. Photon.* **10**, 180 (2016).
- [31] I. L. Garanovich, A. A. Sukhorukov, and Yu. S. Kivshar, Defect-free Surface States in Modulated Photonic Lattices, *Phys. Rev. Lett.* **100**, 203904 (2008).
- [32] A. Szameit, I. L. Garanovich, M. Heinrich, A. A. Sukhorukov, F. Dreisow, T. Pertsch, S. Nolte, A. Tunnermann, and Yu. S. Kivshar, Observation of Defect-free Surface Modes in Optical Waveguide Arrays, *Phys. Rev. Lett.* **101**, 203902 (2008).
- [33] W. P. Su, J. R. Schrieffer, and A. J. Heeger, Solitons in Polyacetylene, *Phys. Rev. Lett.* **42**, 1698 (1979).
- [34] J. K. Asbóth, L. Oroszlány, and A. Pályi, *A Short Course on Topological Insulators*, Lecture Notes in Physics Vol. 919 (Springer, Berlin, 2016).
- [35] Yu. S. Kivshar and S. K. Turitsyn, Spatiotemporal pulse collapse on periodic potentials, *Phys. Rev. E* **49**, R2536 (1994).
- [36] S. Ryu, A. P. Schnyder, A. Furusaki, and A. W. W. Ludwig, Topological insulators and superconductors: Tenfold way and dimensional hierarchy, *New J. Phys.* **12**, 065010 (2010).
- [37] S. Ganeshan, K. Sun, and S. Das Sarma, Topological Zero-energy Modes in Gapless Commensurate Aubry-André-Harper Models, *Phys. Rev. Lett.* **110**, 180403 (2013).
- [38] N. Malkova, I. Hromada, X. S. Wang, G. Bryant, and Z. G. Chen, Transition between Tamm-like and Shockley-like surface states in optically induced photonic superlattices, *Phys. Rev. A* **80**, 043806 (2009).

- [39] N. Malkova and C. Z. Ning, Interplay between Tamm-like and Shockley-like surface states in photonic crystals, *Phys. Rev. B* **76**, 045305 (2007).
- [40] N. Malkova, I. Hromada, X. S. Wang, G. Bryant, and Z. G. Chen, Observation of optical Shockley-like surface states in photonic superlattices, *Opt. Lett.* **34**, 1633 (2009).
- [41] J. Zak, Berry's Phase for Energy-Bands in Solids, *Phys. Rev. Lett.* **62**, 2747 (1989).
- [42] M. Atala, M. Aidelsburger, J. T. Barreiro, D. Abanin, T. Kitagawa, E. Demler, and I. Bloch, Direct measurement of the Zak phase in topological Bloch bands, *Nat. Phys.* **9**, 795 (2013).
- [43] E. J. Meier, F. A. An, and B. Gadway, Observation of the topological soliton state in the Su-Schrieffer-Heeger model, *Nat. Commun.* **7**, 13986 (2016).
- [44] F. Cardano, A. D'Errico, A. Dauphin, M. Maffei, B. Piccirillo, C. de Lisio, G. De Filippis, V. Cataudella, E. Santamato, L. Marrucci, M. Lewenstein, and P. Massignan, Detection of Zak phases and topological invariants in a chiral quantum walk of twisted photons, *Nat. Commun.* **8**, 15516 (2017).
- [45] E. Flurin, V. V. Ramasesh, S. Hacohe-Gourgy, L. S. Martin, N. Y. Yao, and I. Siddiqi, Observing Topological Invariants Using Quantum Walks in Superconducting Circuits, *Phys. Rev. X* **7**, 031023 (2017).
- [46] C. He, M. H. Lu, W. W. Wan, X. F. Li, and Y. F. Chen, Influence of boundary conditions on the one-way edge modes in two-dimensional magneto-optical photonic crystals, *Solid State Commun.* **150**, 1976 (2010).